Stop-less Lyot coronagraph for exoplanet characterization: first on-sky validation in VLT/SPHERE

Vigan, A., N'Diaye, M., Dohlen, K., Beuzit, J.-L., Costille, A., et al.

A. Vigan, M. N'Diaye, K. Dohlen, J.-L. Beuzit, A. Costille, A. Caillat, A. Baruffolo, P. Blanchard, M. Carle, M. Ferrari, T. Fusco, L. Gluck, E. Hugot, M. Jaquet, M. Langlois, D. Le Mignant, M. Llored, F. Madec, D. Mouillet, A. Origné, P. Puget, B. Salasnich, J.-F. Sauvage, "Stop-less Lyot coronagraph for exoplanet characterization: first on-sky validation in VLT/SPHERE," Proc. SPIE 9912, Advances in Optical and Mechanical Technologies for Telescopes and Instrumentation II, 991226 (22 July 2016); doi: 10.1117/12.2231098

SPIE.

Event: SPIE Astronomical Telescopes + Instrumentation, 2016, Edinburgh, United Kingdom

Stop-less Lyot coronagraph for exoplanet characterization: first on-sky validation in VLT/SPHERE

A. Vigan[a], M. N'Diaye[b], K. Dohlen[a], J.-L. Beuzit[c,d], A. Costille[a], A. Caillat[a], A. Baruffolo[e], P. Blanchard[a], M. Carle[a], M. Ferrari[a], T. Fusco[a,f], L. Gluck[c,d], E. Hugot[a], M. Jaquet[a], M. Langlois[g], D. Le Mignant[a], M. Llored[a], F. Madec[a], D. Mouillet[c,d], A. Origné[a], P. Puget[c,d], B. Salasnich[e], J.-F. Sauvage[a,f]

[a] Aix Marseille Université, CNRS, LAM (Laboratoire d'Astrophysique de Marseille) UMR 7326, 13388, Marseille, France
[b] Space Telescope Science Institute, 3700 San Martin Drive, Baltimore MD 21218, USA
[c] Université Grenoble Alpes, IPAG, F-38000 Grenoble, France
[d] CNRS, IPAG, F-38000 Grenoble, France
[e] INAF - Osservatorio Astronomico di Padova, Vicolo dell'Osservatorio 5, 35122 Padova, Italy
[f] ONERA, The French Aerospace Lab BP72, 29 avenue de la Division Leclerc, 92322 Châtillon Cedex, France
[g] CRAL, UMR 5574, CNRS, Université Lyon 1, 9 avenue Charles André, 69561 Saint Genis Laval Cedex, France

ABSTRACT

The VLT/SPHERE instrument includes a unique long-slit spectroscopy (LSS) mode coupled with Lyot coronagraphy dedicated to the spectral characterization of directly imaged giant exoplanets. The performance of this mode is limited by its non-optimal coronagraph, but in a previous work we demonstrated that it could be significantly improved at small inner-working angles using the stop-less Lyot coronagraph (SLLC). A prototype of the SLLC was installed in VLT/SPHERE in 2014 during the reintegration of the instrument in Paranal, and it was extensively tested in 2015 to characterize its performance. The performance is tested in both imaging and spectroscopy using data acquired on the internal source of SPHERE. In imaging, we obtain a raw contrast gain of a factor 10 at 0.3" with the SLLC. We also demonstrate that no Lyot stop is required to reach the full performance, which validates the SLLC concept. Comparison with a realistic simulation model shows that we are currently limited by the internal phase aberrations of SPHERE. In spectroscopy, we obtain a gain of 1 mag in a limited range of angular separations. Simulations show that although the main limitation comes from phase errors, the performance in the non-SLLC case is very close to the ultimate limit of the LSS mode. We present the very first on-sky data with the SLLC, which appear extremely promising for the future scientific exploitation of an apodized LSS mode in SPHERE. Finally, we explore a new possibility for the speckle subtraction in the LSS mode that could significantly improve the data analysis with respect to methods based on spectral differences.

Keywords: High-contrast spectroscopy, Long-slit spectroscopy, Coronagraphy, Apodization, Exoplanets

1. INTRODUCTION

The new generation of high-contrast imagers and spectrograph has been designed to provide high-contrast at small angular separation through extreme adaptive optics (XAO) systems[1,2] and efficient coronagraphs,[3,4] with the main science objective of detecting and characterizing young giant planets. The back-end science subsystems of these instruments generally include spectroscopic capabilities that are made possible by diffraction-limited integral field spectroscopy (IFS).[5] This provides multi-spectral data allowing very efficient reduction of the speckle-noise through differential imaging techniques[6,7] and enables the possibility to reach unprecedented contrasts.[8]

Send correspondence to A. Vigan: arthur.vigan@lam.fr

Advances in Optical and Mechanical Technologies for Telescopes and Instrumentation II, edited by Ramón Navarro, James H. Burge, Proc. of SPIE Vol. 9912, 991226
 · doi: 10.1117/12.2231098

These new instruments will hopefully provide insight into the population of giant planets, their composition, and evolution.

The Spectro-Polarimetric High-contrast Exoplanet REsearch (SPHERE) planet-finder instrument installed at the VLT[9] is a highly specialized instrument, dedicated to high-contrast imaging and spectroscopy of young giant exoplanets. It is based on the SAXO extreme adaptive optics system,[1,10,11] which controls a 41×41 actuators deformable mirror and four control loops (fast visible tip-tilt, high-orders, near-infrared differential tip-tilt, and pupil stabilization). The common path optics employ several stress polished toric mirrors[12] to transport the beam to the coronagraphs and scientific instruments. Several types of coronagraphic devices for stellar diffraction suppression are provided, including apodized pupil Lyot coronagraphs[4] and achromatic four-quadrant phase masks.[13]

In the near-infrared, SPHERE includes two scientific subsystems: an IFS[14] and the infrared dual-band imager and spectrograph (IRDIS).[15] The latter is a versatile instrument that includes dual-band imaging[16] for the detection of exoplanets and long-slit spectroscopy (LSS) coupled with Lyot coronagraphy for their characterization.[17] The LSS mode provides some unique capabilities in the high-contrast instrumentation world, the main one being that it allows reaching resolutions 5 to 10 times higher than an IFS. However, it comes with some drawbacks such as the requirement to perform field-stabilized observations, resulting in a less stable point-spread function (PSF) and a suboptimal coronagraph, where the coronagraphic mask and the slit are merged into a single device. Another weak point is that a well-optimized Lyot stop cannot be achieved in this mode.

In our previous work,[18] we proposed to use the concept of the stop-less Lyot coronagraph (SLLC)[19,20] to improve the performance of the LSS mode. The SLLC is an apodizer optimized to essentially remove the need for any Lyot stop, at the cost of a reduced throughtput (37% in a design for SPHERE), an enlarged inner-working angle (4.53 λ/D, with λ the wavelength and D the telescope diameter), and a decreased theoretical contrast with respect to an Apodized Pupil Lyot Coronagraph (APLC) that is optimized for imaging.[4] Nonetheless, the simulations presented in Vigan et al. (2013)[18] promise a significant gain at small angular separations (0.2–0.5″), making the SLLC concept an attractive solution to improve the performance of the LSS mode.

The current paper presents the design and manufacturing of the first SLLC prototype, as well as its testing and validation within the SPHERE instrument and some future prospects for the data analysis in LSS. In Sect. 2 we remind the specifications and manufacturing of the SLLC prototype; in Sect. 3 we present the performance in imaging and spectroscopy; finally in Sect. 4 we present the first on-sky results and we briefly discuss a powerful strategy for LSS data analysis.

2. SPECIFICATION AND MANUFACTURING OF THE SLLC

2.1 Specifications

The methods for calculating and optimizing the SLLC apodizer transmission profile are presented in Vigan et al. (2013).[18] The nominal profile was calculated for the H-band (1600 nm) assuming a coronagraphic mask of radius 200 mas on-sky. The VLT central obscuration (14% in pupil diameter) is taken into account in the optimization, but the spiders were not considered to avoid an asymmetric apodization shape. Indeed, such shapes cannot be considered here because the observations are performed in a field-stabilized mode to maintain the object of interest inside the slit, resulting in a rotation of the pupil during the observations. The nominal amplitude transmission (transmission of the electric field amplitude) profile and expected theoretical performance are presented in Fig. 1.

The ultimate performance of the apodizer is driven by its transmission profile, which needs to be as close as possible to the specification. Continuous gray apodizers have traditionally been approximated by binary apodizers created using a halftone-dot process.[21,22] The variable pixel density allows controlling the local transmission, and the transformation from a continuous two-dimension (2D) transmission map to a binarized version is performed using a simple error diffusion algorithm,[23] that is, the same type of algorithm as is used in offset printing to render grayscale levels using only black ink. As demonstrated by Martinez et al. (2009a),[21] this technology is able to produce apodizers with the required amplitude transmission with less than 4% of absolute error. For reference, the tolerance on the specifications for the apodizers used in the APLC of SPHERE were also below 2.5% of error on the amplitude transmission.[24,25]

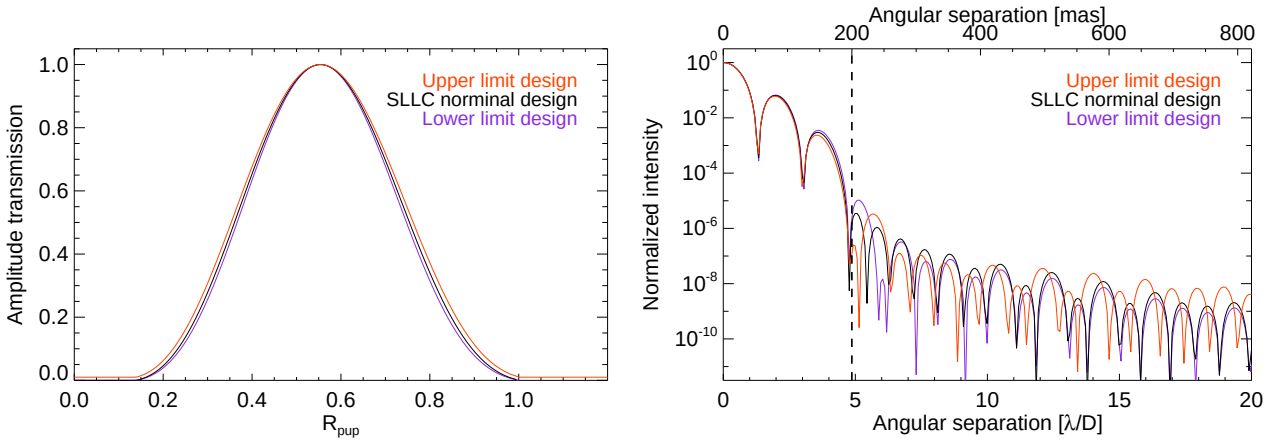

Figure 1. *Left:* Amplitude transmission profile for the nominal SLLC design together with upper and lower limits for manufacturing as a function of the telescope pupil radius. *Right:* Radial intensity profile of the coronagraphic images with the nominal SLLC design together with upper and lower limits, calculated at a wavelength $\lambda = 1600$ nm. The physical edge of the IRDIS coronagraphic mask in LSS mode is represented as a dashed line at 200 mas.

With these constraints in mind, we investigate changes in the amplitude transmission profile and measure the impact on the expected contrast performance. Because the nominal profile is Gaussian-like, we alter the profile by multiplying it with Gaussian functions with varying standard deviation and centered on the peak of the transmission of the nominal profile ($r_{\max}$). The nominal profile can be either attenuated using a function of the form

$$d_{\text{low}} = e^{-0.5\left(\frac{r-r_{\max}}{\sigma}\right)^2}, \tag{1}$$

or amplified using a function of the form

$$d_{\text{up}} = 2 - e^{-0.5\left(\frac{r-r_{\max}}{\sigma}\right)^2}, \tag{2}$$

where r is the radial position and σ the standard deviation of the Gaussian. We vary the value of σ to induce variations of up to 2.5% in the absolute amplitude transmission.

We noted in our initial simulations for Vigan et al. (2013)[18] the importance of the level of the transmission profile at the edge of the pupil (outer edge or central obscuration edge). The SLLC has a very strong apodization function that provides a significant attenuation of the diffraction. This, in part, comes from the fact that there is no transmission *step* at the edges of the pupil, producing a very smooth transition. This condition was also taken into account when defining the tolerance on the transmission profile for manufacturing: we tested modifications of the nominal profile where the minimum transmission was offset by constant values.

In Fig. 1 we present the final tolerances that were adopted for the manufacturing, and the expected performance compared to the performance of the nominal profile. We allow a transmission of 1% for the upper limit at the edge of the pupil. This tolerance is extended outside of the pupil and within the central obscuration to simplify manufacturing and to provide robustness against pupil misalignment. With these tolerances, we expect no measurable change in the final performance (factor <1.5 on average).

2.2 Manufacturing of the apodizer

As mentioned in Sect. 2.1, gray apodizers can easily be manufactured using a microdot process (also known as halftone-dot process), where an array of "pixels" is deposited on a transparent substrate using lithography of a light-blocking metal layer. The density of pixels is varied to obtain the required transmission of the apodizer. A dedicated study of this technology has been performed by Martinez et al. (2009a),[21] which demonstrated that this technology is perfectly suitable to produce the apodizers required by APLCs, without negative impact on

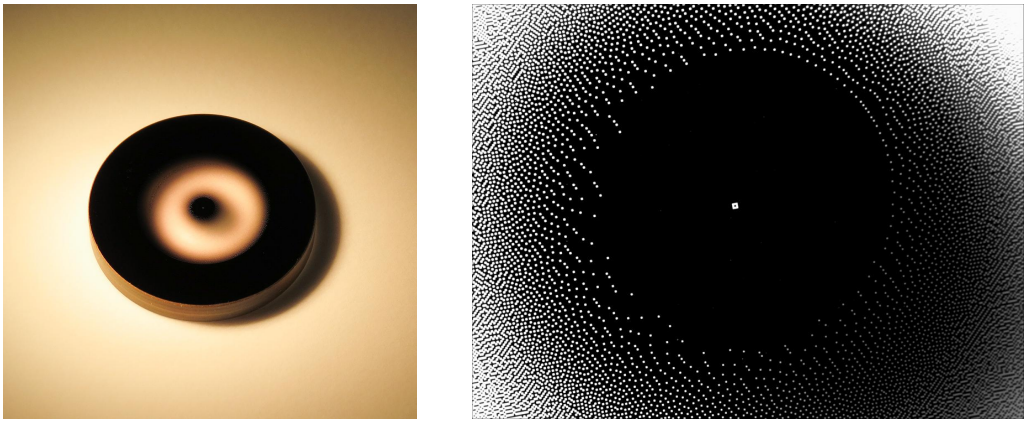

Figure 2. Chromium oxide SLLC prototype during its visual inspection in a clean room at LAM (left) and under a binocular microscope (right). The final SLLC component installed in SPHERE was a second prototype using an aluminum metal layer for the microdots pattern, which increases the optical density in the near-infrared compared to the chromium oxide prototype (see Sect. 2.3).

the final coronagraphic performance. New-generation high-contrast imaging instruments SPHERE, P1640, and GPI[9,26,27] used APLC apodizers that were manufactured with this technology.

For the SLLC, the same technology was foreseen for the manufacturing of the prototype, but some uncertainties remained on the choice of the material to use for the metallic deposit because of the need for an extremely high optical density (>OD4 in amplitude, i.e., 10^4 attenuation) that would allow us to achieve sufficiently close to zero transmission at the edge of the pupil. As a consequence, two SLLC prototypes were manufactured by Aktiwave LLC in Rochester, NY, USA. The substrates were made of fused-silica, on which a layer of chromium oxide was deposited for the first prototype and a layer of aluminum for the second one. The thickness of the metal layer was optimized for both metals to obtain an optical density of 4. Possible phase shift effects induced by the metal layer were not taken into account for the optimization of the pattern and its thickness. Photolithography of the metal layer was performed using a mask containing square pixels of 20 μm in size, the density of which was optimized by Aktiwave to produce the required transmission curve. Finally, an anti-reflection coating ensuring a reflectivity R<1% over the 950–2320 nm range was deposited on the other side of the substrates.

The manufactured components were received at *Laboratoire d'Astrophysique de Marseille* (LAM) in 2014, where they underwent a visual inspection to check for any obvious defects. A picture of the chromium oxide prototype during its inspection is shown in Fig. 2, with a close-up on its central part where a square pattern was introduced on purpose to allow precise centering of the apodizer in its mechanical mount. The infrared transmission profiles provided by Aktiwave agreed well with the specifications for transmissions >20%, but lower transmissions could not be measured precisely.

2.3 Transmission measurement

The SLLC prototypes were installed and quickly tested inside SPHERE during the reintegration of the instrument at the Paranal observatory in early April 2014. The transmission of both prototypes was measured by acquiring pupil images using the IRDIS pupil imaging mode. For each transmission measurement, three images are acquired: (1) a clear pupil image without the SLLC, (2) an apodized pupil image with the SLLC, and (3) a background frame with the light source switched off. Particular care was taken to adjust the integration time so as to avoid any saturation in the images. Images were acquired at four different wavelengths, with broad-band Y ($\lambda = 1043$ nm, $\Delta\lambda = 70$ nm), J ($\lambda = 1245$ nm, $\Delta\lambda = 120$ nm), H ($\lambda = 1625$ nm, $\Delta\lambda = 145$ nm), and K_s ($\lambda = 2180$ nm, $\Delta\lambda = 150$ nm) filters. The clear and apodized pupil images were background subtracted, and the bad pixels were corrected using a sigma-clipping procedure. Then, the apodized pupil image was divided by the clear pupil image to obtain the transmitted intensity. Finally, mean azimuthal profiles were calculated starting from the center of the pupil. Amplitude transmission measurements in $H-$band for the two prototypes are presented in Fig. 3.

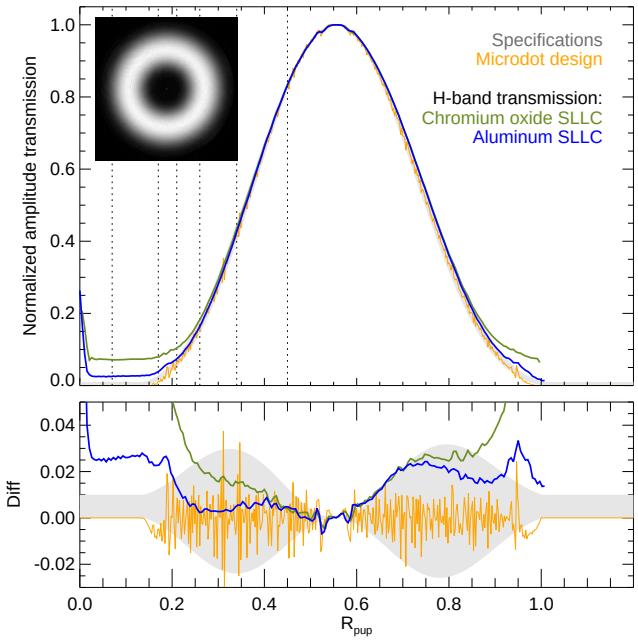

Figure 3. Azimuthal average of the amplitude transmission in H band for the chromium oxide (green) and aluminum (blue) SLLC prototypes as a function of the normalized distance from the apodizer center (R_{pup}). The increase in transmission close to zero corresponds to the pattern introduced in the design to facilitate the opto-mechanical centering of the apodizer. The design specifications are represented by a gray envelope. The transmission of the microdots map designed by Aktiwave is also plotted in orange. This profile appears noisier because the microdots map is binarized. The top plot shows the normalized transmission measurement, and the bottom plot shows the error with respect to the nominal transmission profile. The vertical dotted lines correspond to the radii where we plot the transmission as a function of wavelength in the left panel of Fig. 4. The transmission map of the aluminum prototype in H band is shown as an inset in the top left corner of the plot.

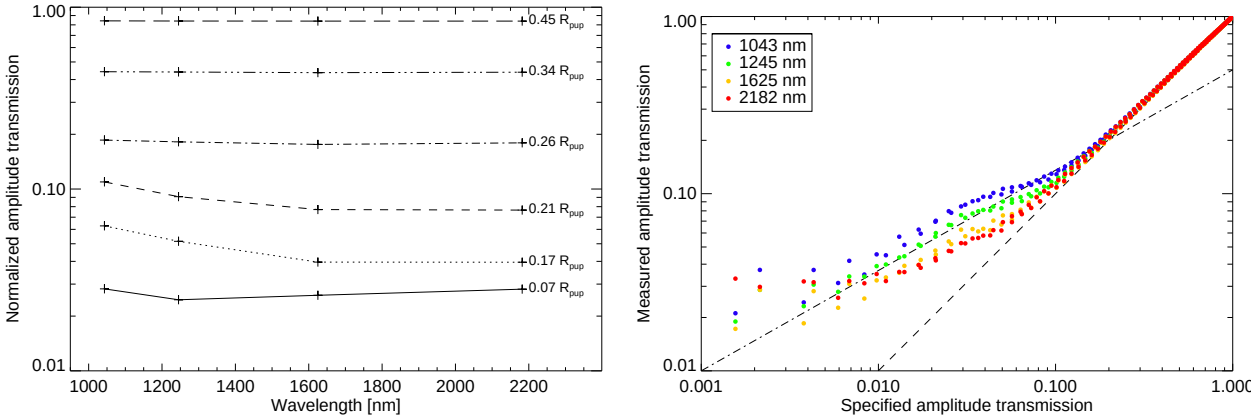

Figure 4. Chromaticity of the amplitude transmission of the aluminum prototype. *Left:* Normalized amplitude transmission as a function of wavelength at different radii in the pupil (dotted vertical lines in Fig. 3), for which the value is indicated on the right side of each curve. *Right:* Measured amplitude transmission at the four wavelengths as a function of the original specification. The dashed and dash-dotted lines show the 1 decade/decade and 0.5 decade/decade trends.

From the very first measurements it appeared that the chromium oxide prototype did not meet the specifications in the low-transmission part (<20%) of the apodizer. Because only one free position was available in the SPHERE apodizer wheel and because limited time was available for extensive tests during the reintegration period, we chose to keep the aluminum prototype inside the instrument, which is closer to the specifications. For this reason, we do not discuss the results from the chromium oxide prototype in more detail, and we refer to Vigan et al. (2014)[28] for some additional information and measurements. From now on, we refer only to the aluminum prototype.

For the aluminum prototype, the transmission is closer to the specifications, but there are still some problems in the low-transmission parts of the apodizer. The minimum transmission obtained in the central part and at the edge of the pupil is ∼2.5%. This measurement illustrates the difficulty of manufacturing apodizers for the near-IR with very high optical densities, as was already identified by previous studies in the context of the GPI instrument.[29]

A microdots apodizer relies on the absorption and diffraction of light by small (20 μm in our case) metallic dots deposited on a substrate whose distribution is such that the density of dots produces the required transmission profile. As detailed by Dorrer et al. (2007),[23] the spatial filtering produced by the following optical train, that is, by the field-stop located in the coronagraph mask plane in SPHERE, causes the intensity distribution in the relayed image of the apodizer to be the square of its near-field transmission function, regardless of the wavelength. The specified near-field transmission should therefore be equal to the desired amplitude transmission function.

The measurements made on the SLLC prototype in SPHERE indicate that this theory breaks down for low-transmission values, where the expected transmission is no longer achieved (Fig. 3) and a clear chromatic behavior is observed (Fig. 4). An indication of what happens can be gained from the right panel of Fig. 4, where we plot the measured amplitude transmission versus the specified amplitude transmission, in which we identify three distinct transmission regions:

1. Amplitude transmission above around 15%: The slope equals 1 decade/decade for all wavelengths, hence fully validating the Dorrer et al. (2007)[23] theory and producing a gray apodization function as expected.

2. Amplitude transmission below 15%, down to around 1%: The transmission is higher than expected and has a notable blue tint. The slope of the curves tend toward 0.5 decade/decade. In this range, the absorbing dots agglomerate into fully opaque patches, leaving only isolated dot-sized holes. Spatial filtering therefore operates on the transmitted and not on the absorbed light, so that the measured intensity is now proportional to the near-field apodizer transmission. The effect of this is to make the measured amplitude transmission equal to the square root of the specified electric field transmission, as observed.

3. Amplitude transmission below 1%: Here, the apodizer is essentially fully covered with the aluminum film, and we measure the transmission of the materiel itself. The measured intensity transmission saturates at around 10^{-3}, representing an optical density of 3, and has a slightly red tint.

These measurements are particularly interesting for the future development of apodizer prototypes that require very low transmissions. In particular, they highlight the fact that the production of a transmission map based on a simple error-diffusion algorithm may not always be appropriate, and that further considerations are required to produce a transmission profile within tight specifications.

For the parts where the transmission is >15%, the lower panel of Fig. 3 shows that the profile is mostly within specifications, but we can identify two distinct regimes as a function of the pupil radius: (1) for $R_{pup} < 0.56$, which corresponds to the peak of the transmission, the profile is close to the expected transmission given by the microdots map, and (2) for $R_{pup} > 0.56$ the profile is just within specification, but it departs from the profile given by the microdots map. The most likely explanation is that the physical size of the apodizer does not exactly match that of the pupil in the apodizer plane (18 mm in diameter from design). The diameter of the pupil has been measured to be 385.2 pixel in the IRDIS focal plane. We cannot physically measure the diameter of the pupil in the apodizer plane, but we note that if we modify the measured value by only 1 pixel (386.2 pixel, i.e., an increase of 0.26%), the measured azimuthal average falls well within the specification for $R_{pup} > 0.56$. While a pupil diameter of 386.2 pixel is not compatible with our measurements of the pupil size on the IRDIS

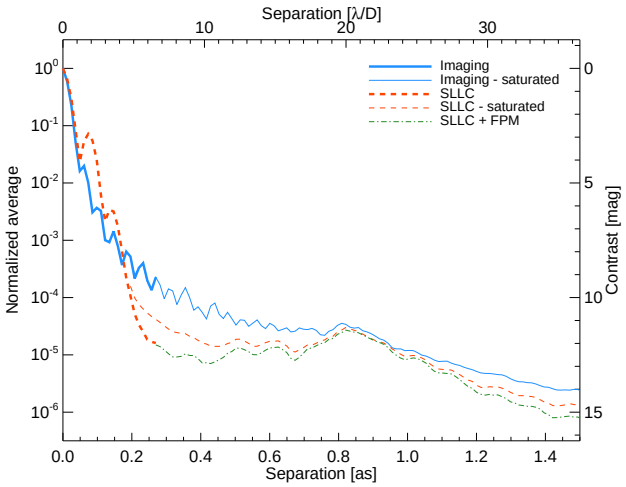

Figure 5. Normalized azimuthal average profiles as a function of angular separation for the imaging data (blue), the SLLC data (red), and the SLLC+FPM data (green) at 1593 nm. The saturated and unsaturated data overlap in the 0.20–0.25″ range. The data with the FPM plane mask is also plotted starting at 0.25″.

detector, it can be translated into the apodizer plane. In this plane, a difference of only 47 μm (0.26% of 18 mm) between the physical pupil diameter and the specification is enough to produce the change. Such a small error on the size of the beam is plausible in the system and agrees with the tolerances.

A final important measurement is the total intensity transmission of the prototype, which we measure to be $22.9\% \pm 0.7\%$ using the four wavelengths. This is a significant attenuation that is directly related to the very strong apodization function of the SLLC, but also to a peak amplitude transmission (at $r_{\max}$) of only 83% instead of >95% as originally specified. The origin of this discrepancy has not been identified by the manufacturer.

3. SLLC PERFORMANCE IN IMAGING AND SPECTROSCOPY

3.1 Imaging

The SLLC apodizer was first tested with SPHERE/IRDIS in imaging to understand its performance and limitations. The data were acquired with SPHERE on August 31, 2015 during daytime technical time. All measurements were made internally using the light sources available in the calibration unit of the instrument.[30] For imaging, the data consisted of two sets with and without the apodizer. In each set, a deep reference PSF in the H2 filter ($\lambda = 1593$ nm, $\Delta\lambda = 26$ nm) of IRDIS was acquired with a neutral density (ND) filter of value 3.5, which provides an attenuation of a factor 955 of the flux in this filter. Then a saturated PSF was acquired by changing to a ND of 1.0 (attenuation of a factor 7.2 in filter H2). Finally, for imaging with the SLLC, an additional image was acquired with a circular, suspended focal-plane mask (FPM) of diameter 0.45″ (but no Lyot stop) to validate the SLLC concept. Corresponding calibrations were also acquired: background frames with the same integration time as the science data, and a flat-field to correct for inter-pixel sensitivity variations.

The data were all processed in a similar fashion. Master backgrounds, bad-pixel maps and flat-fields were created using the v0.15.0 release of the SPHERE data reduction and handling software.[31] Each image was first background subtracted and then divided by the flat field. Bad pixels identified in the flat and backgrounds were corrected by replacing them with the median of neighboring good pixels. Then the images were normalized by their integration time, and the attenuation of the ND was also compensated for to be able to compare the images taken with different ND filters. The saturated and unsaturated images were aligned together manually using the Airy rings and speckles, providing an accuracy of ∼0.1 pixel. The SLLC image with a FPM was also aligned with respect to the saturated SLLC image. Finally, azimuthal average profiles were calculated on each of the images.

The resulting contrast curves for the different data are showed in Fig. 5, which shows the azimuthal average profile for the imaging data, the SLLC data and the SLLC+FPM data, normalized in each case to the maximum

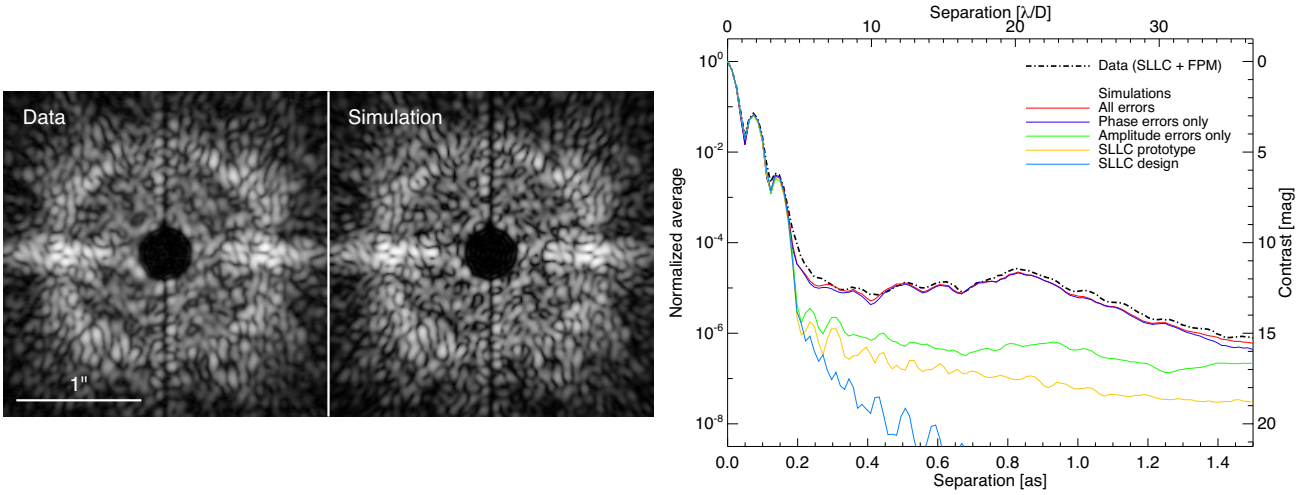

Figure 6. *Left:* Comparison of SLLC+FPM imaging data acquired in the IRDIS H2 filter with the output of our SPHERE simulation model. The vertical dark line at the center corresponds to the arms that hold the suspended FPM. The spatial extension is 2.6″ on the side. *Right:* Normalized azimuthal average for different simulations in the H2 filter (1593 nm) with the SLLC and taking into account various error terms: all sources of errors (red), only phase errors (dark blue), only amplitude errors (green), only the measured transmission map of the SLLC prototype (orange), and finally with only the SLLC nominal design (light blue). The SLLC+FPM data are overplotted as a black dash-dotted line.

of the unsaturated PSF acquired in the same instrumental configuration. The saturated and unsaturated data overlap in the 0.20–0.25″ range, and the SLLC+FPM data are plotted starting at 0.25″.

For the unsaturated data, we see the change of shape of the SLLC PSF, with the characteristic two bright Airy rings that were visible in Fig. 1, followed by a steep drop of the PSF profile down to slightly over 10^{-5} at 0.25″ ($\sim 6\ \lambda/D$). This is different from the imaging data, for which the PSF follows a classical Airy pattern, reaching slightly over 10^{-4} at 0.25″. At this radius we thus obtain a factor ∼10 in raw contrast. The saturated data are less straightforward to interpret from the azimuthal average of the SLLC data. While the saturated and unsaturated imaging data match exactly, the level of the SLLC saturated data is slightly higher in the 0.20–0.25″ range than the unsaturated SLLC data. The origin of this difference is stray light close to the optical axis because the PSF core is highly saturated. When removing this stray light with a high-pass filter, the saturated curves falls back to the level of the non-saturated curve and the SLLC+FPM curve. This plot shows that the SLLC delivers a gain by a factor 10 at 0.3″ and 5 at 0.5″, which is on the order of our predictions in Vigan et al. (2013)[18] in the presence of a realistic amount of aberrations (>50 nm rms).

Finally, we also compared the saturated data with the data acquired with SLLC+FPM. In this data set, we did not use a Lyot stop, that is, we only used the FPM as an anti-saturation device. The azimuthal standard deviation curve exactly matches the one from saturated imaging, which means that we obtain an identical performance in the two configurations. This is a validation of the SLLC concept: it shows that with this device, we do not need to use a Lyot stop to remove diffraction, contrary to the classical Lyot coronagraph (CLC) or APLC, for which both a FPM and a Lyot stop are necessary to achieve complete diffraction suppression.

To assess the performance of the SLLC in imaging, we constructed a simple simulation model of the instrument. We refer the reader to Vigan et al. (2016)[32] for a complete description of the model. The model uses as input an intensity map of the pupil and a transmission map of the SLLC apodiser measured in the instrument, and an OPD map measured using the ZELDA[33,34] wavefront sensor prototype of SPHERE. The inputs are used in our Fourier-based simulation model of the instrument to obtain images that can be compared to the data acquired in SPHERE/IRDIS. Figure 6 (left) shows a comparison of the data to the results of our simulation in the case of SLLC+FPM data including both phase and amplitude errors. Figure 6 (right) shows the corresponding contrast plot, with a decomposition of the different error terms, compared to the SLLC+FPM data presented in Fig. 5.

The visual agreement in Fig. 6 is excellent: all the main structures are visible, and many common speckles or groups of speckles can be identified between the data and simulation. The match is not perfect, however, certainly because the inputs of our model are not perfect measurements. In particular, the phase map measured with ZELDA does not exactly represent the aberrations within the system because of the dead or stuck actuators of the SPHERE deformable mirror. In addition, our model does not include either chromatic effects or Fresnel propagation effects. Even though these effects are expected to be small in SPHERE,[35] they might contribute slightly at the level of individual speckles. Finally, ZELDA only measures the aberrations upstream of the coronagraph, which means that the aberrations introduced downstream are not taken into account. For IRDIS, these aberrations amount to a maximum of ∼21 nm rms (see error budget in Dohlen et al. 2008[15]).

The normalized average profile also showed in Fig. 6 confirm that the model is nonetheless very good. There is an excellent match between the data and the profile that includes all error terms (phase and amplitude errors, and the measured SLLC transmission map), which proves that our SPHERE simulation model is enough to understand the current limitations of the SLLC in SPHERE. Clearly, the highest contribution comes from the phase errors in the range 4–30 λ/D, with the amplitude errors being a factor 5 to 20 lower, depending on the angular separation. At separations ¿35 λ/D, the amplitude errors start to be noticeable, but hopefully they are mostly static and their contribution can be removed through differential imaging. The contribution of the transmission of the SLLC prototype is mostly negligible above contrast ratios of 10^{-6}, but we see a significant departure between the performance with the measured profile and with the nominal design.

3.2 Spectroscopy

The LSS data were acquired on the same day and in the same conditions as the imaging data. We acquired two data sets in the low-resolution spectroscopy (LRS) mode of IRDIS, one with the SLLC and one without. In this mode, a slit is located in the coronagraphic focal plane. It has a width of 0.12″ and includes a central FPM of radius 0.20″. The following Lyot pupil plane includes a slightly undersized circular Lyot stop with a size equal to 92% of the pupil diameter. The dispersive element, a double prism, is located immediately after this basic Lyot stop. The double prism and Lyot stop constitute a single opto-mechanical component, and they cannot be decoupled. As a result, we are effectively working with a circular Lyot stop in LSS. However, as demonstrated in Vigan et al. (2013),[18] this stop is not optimized and does not provide efficient diffraction suppression at small separations, which is what triggered the development of the SLLC for the IRDIS/LSS mode. For each data set, we acquired a deep coronagrapic image with the PSF behind the FPM, and an off-axis reference PSF where the PSF is offset inside the slit with respect to the FPM. Necessary calibrations were also acquired: background frames with the same integration time as the science data, a flat-field to correct for inter-pixel sensitivity variations, and a wavelength calibration.

The data were treated in a way very similar to the imaging data, with first a subtraction of the background, then a division by the flat-field, and finally a correction of the bad pixels. The SPHERE pipeline was also used to reduce the wavelength calibration, which allowed us to attribute the corresponding wavelength to each pixel. All spectra were normalized by their integration time, and for the off-axis reference PSF, the effect of the ND filter that was used to avoid saturation was compensated for at each wavelength.

Finally, coronagraphic profiles were extracted at different wavelengths along the spatial dimension and were normalized to the peak of the off-axis reference PSF at the same wavelength. Because LSS provides only a single spatial dimension and a single spectral dimension (contrary to an IFS, for example), it is not possible to calculate an azimuthal average profile. However, to take into account the finite width of the slit (0.12″, or ∼10 pixels on the detector), we averaged the profile along the spectral dimension over a width of 10 pixels to account for all the flux at the considered wavelength.

The results with and without SLLC are compared in Fig. 7. We see again that the data and the simulation match well visually. The comparison of the normalized contrast profiles also show a very good agreement at 1600 nm: the orders of magnitude are the same, and the range of separations where the SLLC brings a gain of ∼1 mag is similar. This gain is clear within 0.2–0.5″, which corresponds approximately to the range where some gain was expected in Vigan et al. (2013).[18] Beyond this range, both profiles are at a very similar level. We note however that the match is not as perfect as for the imaging case, simply because in LSS we only have access to a single spatial dimension, so we cannot calculate an azimuthal average that would smooth the local differences

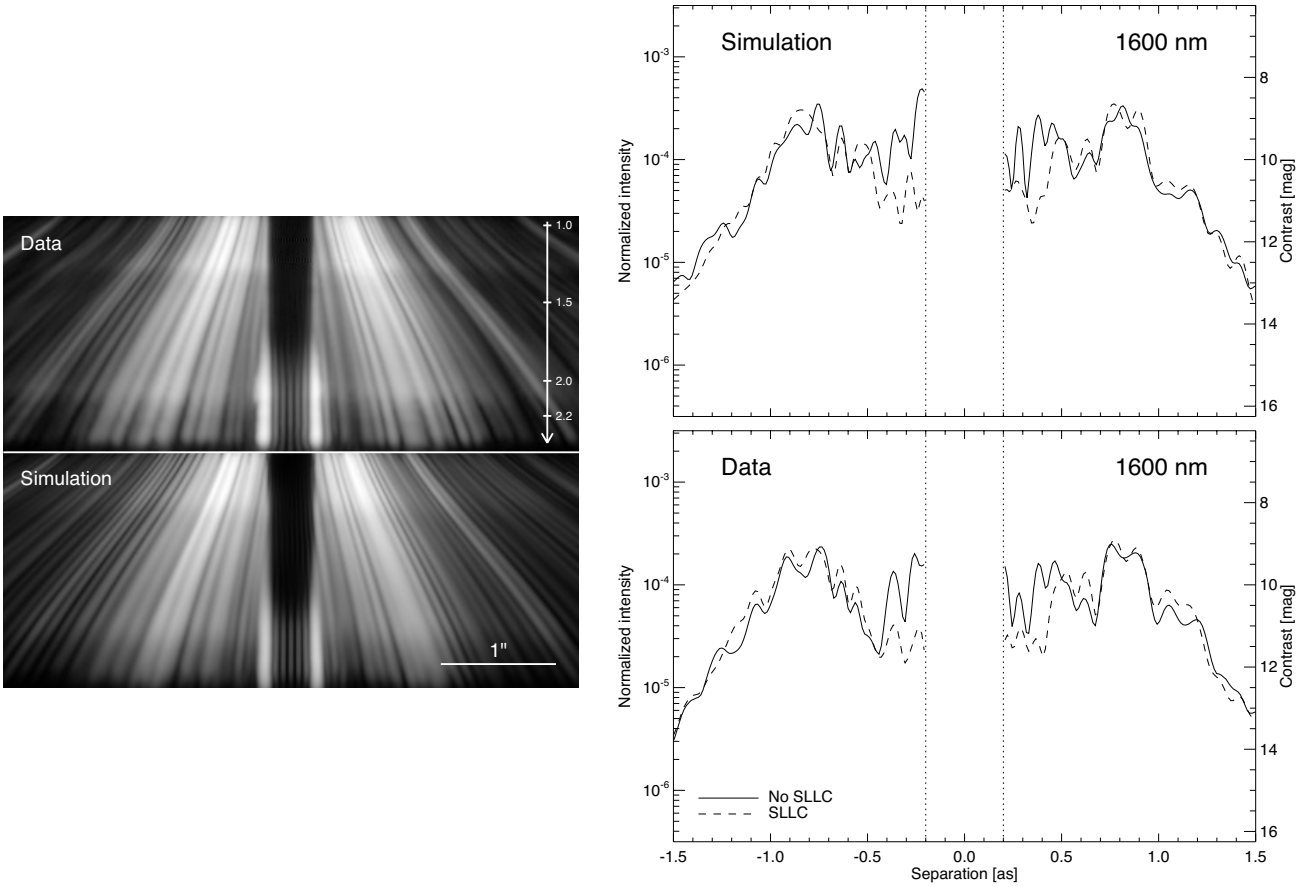

Figure 7. *Left:* IRDIS/LSS data acquired with the SLLC (top) compared to the output of our SPHERE simulation model (bottom). The dark band at the center corresponds to the location of the FPM inside the slit. The wavelength scale (in micron) is indicated with the downward white arrow. The total spectral range is 0.95–2.3 μm, and the spatial extension is 2.5″. *Right:* LSS coronagraphic intensity profiles with (dashed line) and without (plain line) the SLLC as a function of angular separation on both sides of the optical axis and normalized with respect to an off-axis PSF. The top panel presents the data acquired in SPHERE and the bottom panel the simulations performed at the same wavelengths with our SPHERE simulation model including all error terms. The central part between -0.2″ and 0.2″ without any data corresponds to the location of the FPM inside the slit.

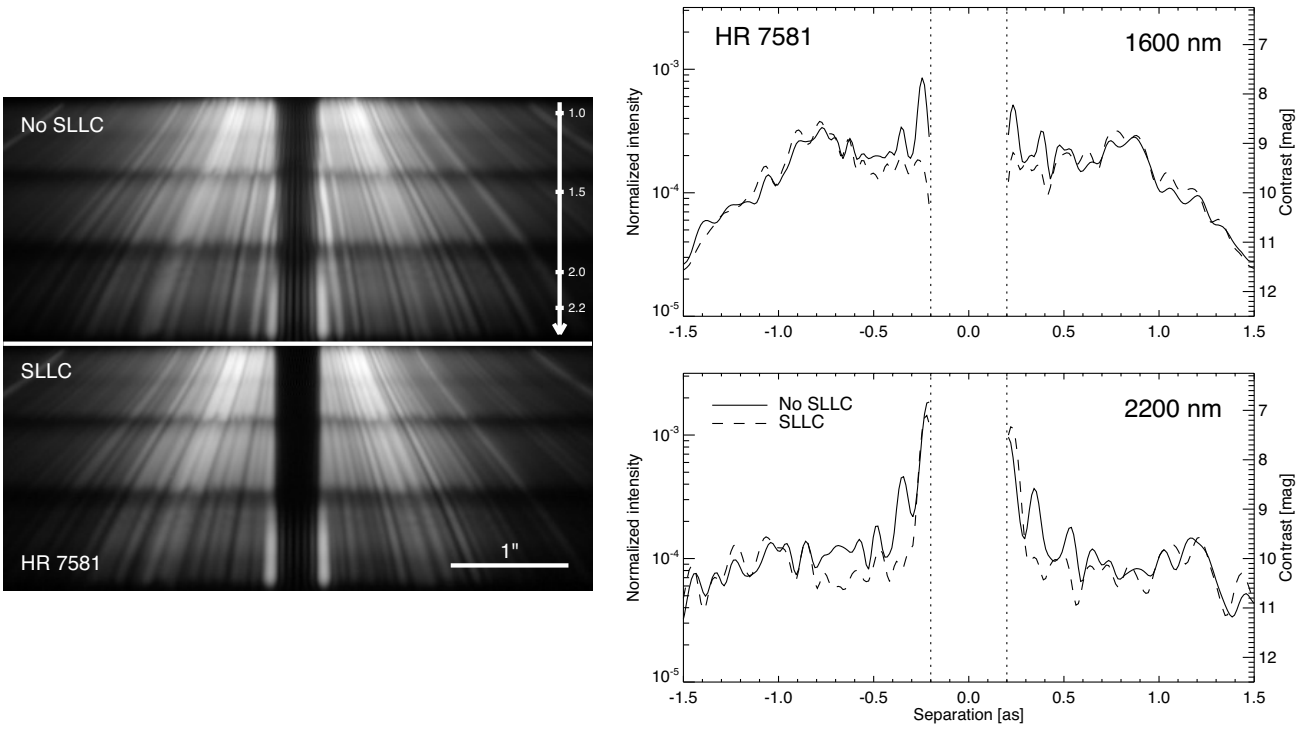

Figure 8. *Left:* On-sky IRDIS/LSS data acquired on the star HR 7581 without (top) and with the SLLC (bottom). The wavelength scale (in micron) is indicated with the downward white arrow. The total spectral range is 0.95–2.3 μm, and the spatial extension is 2.5″. The horizontal dark lines at ∼1.4 μm and ∼1.9 μm correspond to atmospheric absorption bands. *Right:* IRDIS/LSS coronagraphic intensity profiles with (dashed line) and without (plain line) the SLLC as a function of angular separation on both sides of the optical axis and normalized with respect to an off-axis PSF. Profiles are plotted at 1600 nm (H-band) and 2200 nm (K-band).

and only show the underlying speckle field statistics. Indeed, the slit samples only the speckles that are visible along the y-axis in Fig. 6 (the slit is horizontal in SPHERE) and disperses them, so that any difference in the speckle field at that location will be immediately visible in the coronagraphic profile. We have seen in Sect. 3.1 that the speckles are not all exactly reproduced by our simulation, which means that some differences between the data and the simulation are to be expected in LSS.

4. FIRST ON-SKY RESULTS AND FUTURE PROSPECTS FOR LSS DATA ANALYSIS

4.1 On-sky results on HR 7581

The internal measurements presented in the previous sections are encouraging, but they are somewhat disconnected from real-world observations where the amount of residual aberrations from the XAO system (∼65 nm rms) will dominate the overall error budget, and where the diffraction of the telescope central obscuration and spiders will certainly affect the performance.

On the night of October 11, 2015 we had the opportunity of acquiring an on-sky data set with the SLLC for a first "real-world" assessment of the performance. We observed HR 7581, a bright (H = 1.65) star. The observing conditions were average, with a reported DIMM seeing of 0.7–0.9″, a coherence time slightly over 2 ms, and wind blowing from the west at a speed of ∼6 m/s. We obtained two data sets, with and without the SLLC, each data set consisting of 4 min of deep coronagraphic data, 3 min of off-axis reference PSF, and an appropriate set of sky backgrounds. The wavelength calibration and flat fields were acquired in the morning as part of the daily calibrations of the instrument. The spectra with and without SLLC, and coronagraphic profiles at two wavelengths are presented in Fig. 8.

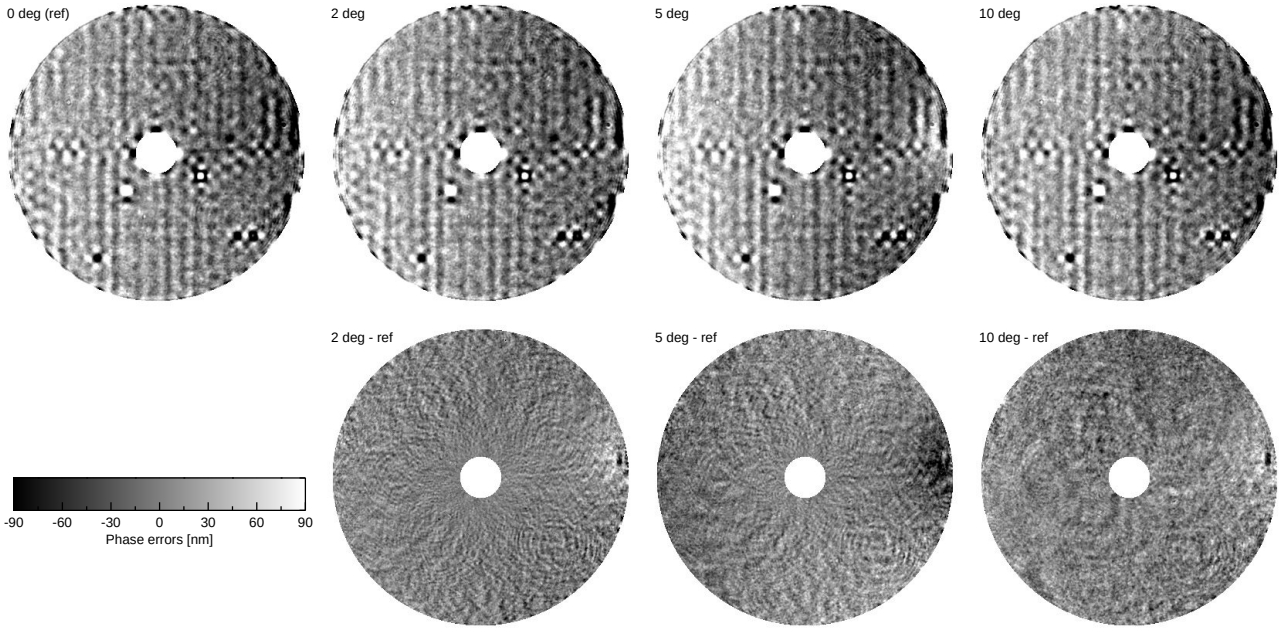

Figure 9. *Top:* OPD maps measured with ZELDA at 4 different orientations of the derotator (0, 2, 5 and 10 deg). *Bottom:* Difference between the 0 deg OPD map (reference) and the 2, 5 and 10 deg OPD maps to show the differential aberrations between close orientations of the derotator.

The non-SLLC and SLLC spectra look visually different at small separations (0.2–0.4″). In this range, the non-SLLC spectrum is dominated by diffraction residuals similar to dispersed, bright, and dark Airy rings. This feature was already noted in the simulations of Vigan et al. (2013)[18] and was identified as the main limitation in the subsequent data analysis required for extracting the spectrum of planetary companions. These diffraction residuals are totally absent from the SLLC spectrum, which looks more or less similar to the data obtained on the internal source and showed in Fig. 7. The contrast plots confirm the presence of the residuals in the non-SLLC data. Even in K-band, where the mode is not fully optimized because of the size of the coronagraphic mask, there is a visible contrast gain of up to 1.5 mag in 0.5–0.7″. In H-band, the gain is slightly smaller but still significant. These findings and the obtained contrasts are perfectly consistent with the results reported in Vigan et al. (2013).[18] This is promising for future scientific results with the SLLC, because in Vigan et al. (2013)[18] we demonstrated that although the raw contrast gain with the SLLC may not be very impressive, the subsequent data analysis based on spectral differential imaging will yield better results when diffraction residuals are eliminated.

The results obtained on the internal source already showed some potential for the SLLC and highlighted the limitations of the current LSS mode. We now see that when considering the full telescope pupil, including both central obscuration and spiders, the difference between the SLLC and non-SLLC is even more accentuated. In the case presented here, the orientation of the pupil was so that the diffraction spikes were far from the slit, so the only remaining possibility is the central obscuration of the telescope. The Lyot stop in the LSS mode is a simple circular diaphragm with a size equal to 92% of the pupil, which does not include any mask for the central obscuration. This is of course a severe limitation for the coronagraphic performance in LSS with the full telescope pupil. By contrast, the SLLC has been optimized by design to take the central obscuration into account (but not the spiders), which directly reflects on the on-sky performance.

4.2 Prospects for LSS data analysis

Even when suppressing efficiently the residual diffraction rings with the SLLC, the data analysis in LSS is a complicated topic because of the lack of spatial information, which requires to rely only on spectral diversity to estimate and remove the speckles.[17] One possibility to improve the data analysis would be to artificially add

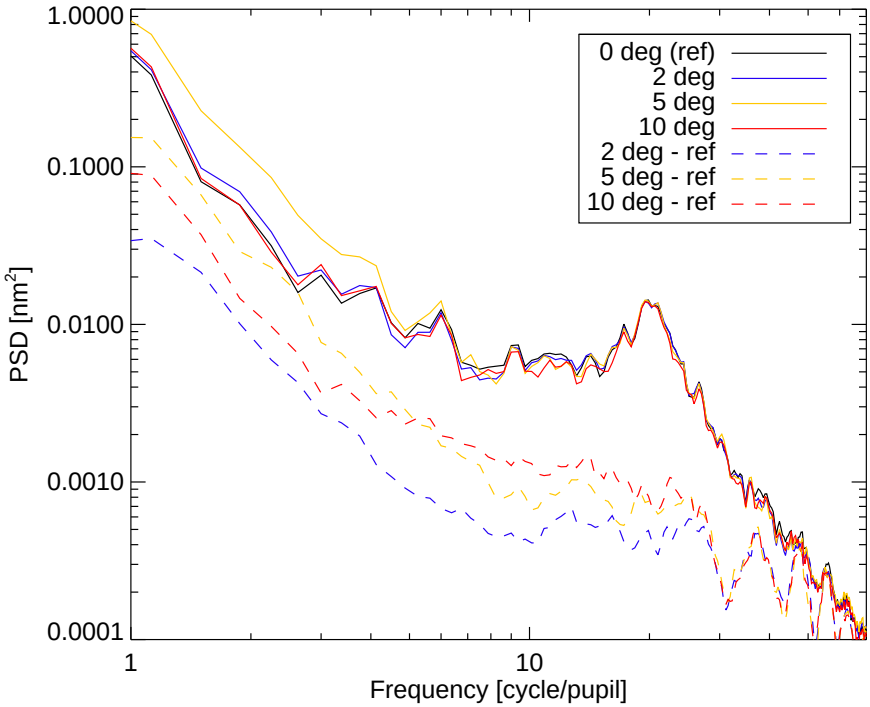

Figure 10. Power spectral density of the OPD maps showed in Fig. 9.

Table 1. Amount of aberrations measured with the ZELDA wavefront sensor at different derotator orientations

Derotator position	Amount of aberrations [nm RMS]
OPD maps	
0 deg (ref)	44.6
2 deg	44.9
5 deg	47.5
10 deg	43.9
Differential OPD maps	
2 deg - ref	19.8
5 deg - ref	22.9
10 deg - ref	22.5

some diversity into the data, e.g. by moving the derotator in order to move the PSF of the companion out of the slit. This artificial ADI has already been used in imaging with previous generations of instruments, but never resulted in major contrast improvements because of the lack of stability of these instruments.[36] However, the overall very high optical quality and stability of the SPHERE optics is a major difference with respect to previous instrumentation. As a consequence, using as reference images taken at a different position angle of the derotator could seriously be considered.

In Fig. 9 top row, we show ZELDA images of the pupil taken at different 4 different orientations of the derotator: 0 deg (reference), 2 deg, 5 deg and 10 deg. And in the bottom row we show the 2, 5 and 10 deg images to which we have subtracted the reference 0 deg image. Table 1 gives the amount of aberrations (in nm RMS) in the original and differential OPD maps, and in Fig. 10 we also show the power spectral density of the original and differential OPD maps. In the individual OPD maps, there is ∼45 nm RMS of aberrations from the calibration light source down to the coronagraphic plane, where the ZELDA mask is located. After subtraction of a reference image at the 0 deg orientation, the differential OPD map contains ∼20 nm RMS of aberrations. In terms of spatial frequencies, we see in Fig. 10 that the attenuation is most effective in the low- and mid-frequencies range (<40 cycle/pupil), leaving mostly untouched the high-frequencies. It means that most of the low-frequencies are common between two derotator positions, or in other words that they do not originate from the derotator. The consequence is that if everything else remains fixed, images taken at different derotator orientations can be used as reference for the speckle subtraction. The exact quantification and limitations of this approach will be studied in details in a future work.

As an experiment for this observing strategy, we performed a test on a data set acquired within the context of the SPHERE GTO time (SHINE survey). The data was acquired on a bright target (both V and H <4) in excellent observing conditions (seeing ∼0.5″), with a total integration time of 60 min. We injected a fake planet inside the data at a separation of 0.45″, with a contrast of 2×10^{-5} with respect to the star. Then the data was analysed with two approaches: the first one is an improvement of the method described in Vigan et al. (2008),[17] which is solely based on spectral differential imaging; in the second, we splited the data in two, injecting the fake planet only in the first half of the data set, and using the second half as reference. With the reference data set, we constructed modes using principal component analysis (PCA) following Soummer et al. (2012).[37] Then the modes were subtracted to the data, and we saved images with an increasing number of subtracted mode. The results are presented in Fig. 11 for both the SDI and PCA-based approaches. It is clear from the images and the extracted spectrum that the PCA-based approach largely outperforms the SDI-based approach. The spectrum extracted from the SDI analysis shows no feature that resemble the original input spectrum. On the contrary, the spectrum extracted from the PCA analysis shows very clear features from the original input spectrum, even though there are some strong over-subtraction effects that would need to be calibrated. These initial tests appear promising for future evolutions in the observaving strategy and data analysis of the LSS mode, which could ultimately be used to characterize much fainter companions than initially anticipated.

ACKNOWLEDGMENTS

The authors would like to thank C. Dorrer from Aktiwave LLC for his contribution on the manufacturing of the apodizer, and M. Kasper and G. Zins for their expert help with the SPHERE AO and control software. MN would like to thank Rémi Soummer and Laurent Pueyo for their support. Finally, the authors are extremely grateful to Andreas Kaufer, Director of La Silla Paranal observatory, for authorizing them to acquire and present the very first on-sky SLLC data.

The SLLC prototypes were funded by the *Action Incitative* program of *Laboratoire d'Astrophysique de Marseille*. AV acknowledges support from the French National Research Agency (ANR) through the GUEPARD project grant ANR10-BLANC0504-01. This work is partially supported by the National Aeronautics and Space Administration under Grants NNX12AG05G and NNX14AD33G issued through the Astrophysics Research and Analysis (APRA) program (PI: R. Soummer). MN would like to acknowledge the ESO Chile Visiting Scientist program.

SPHERE is an instrument designed and built by a consortium consisting of IPAG (Grenoble, France), MPIA (Heidelberg, Germany), LAM (Marseille, France), LESIA (Paris, France), Laboratoire Lagrange (Nice, France),

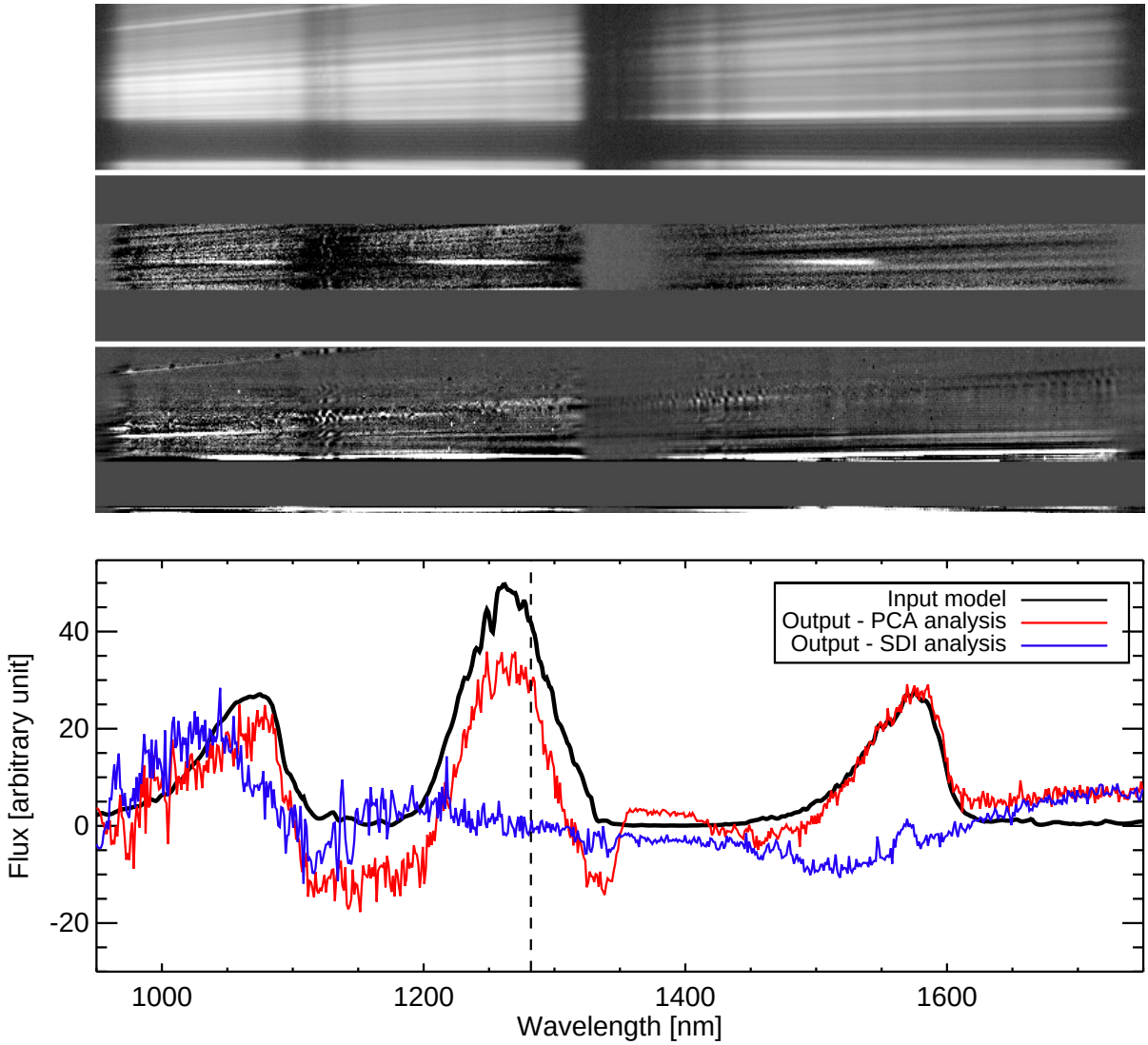

Figure 11. Result of our simulation where we injected a fake planet at $0.45''$ from the star, with a contrast of 2×10^{-5} (top image). The data was then analysed with PCA- and SDI-based approaches (respectively middle and bottom images). The lower panel shows the spectra extracted after the analysis, compared to the input spectrum.

INAF - Osservatorio di Padova (Italy), Observatoire de Genve (Switzerland), ETH Zurich (Switzerland), NOVA (Netherlands), ONERA (France) and ASTRON (Netherlands) in collaboration with ESO. SPHERE was funded by ESO, with additional contributions from CNRS (France), MPIA (Germany), INAF (Italy), FINES (Switzerland) and NOVA (Netherlands). SPHERE also received funding from the European Commission Sixth and Seventh Framework Programmes as part of the Optical Infrared Coordination Network for Astronomy (OPTICON) under grant number RII3-Ct-2004-001566 for FP6 (2004-2008), grant number 226604 for FP7 (2009-2012) and grant number 312430 for FP7 (2013-2016).

REFERENCES

[1] Fusco, T., Rousset, G., Sauvage, J.-F., Petit, C., Beuzit, J.-L., Dohlen, K., Mouillet, D., Charton, J., Nicolle, M., Kasper, M., Baudoz, P., and Puget, P., "High-order adaptive optics requirements for direct detection of extrasolar planets: Application to the SPHERE instrument," *Optics Express* **14**, 7515 (2006).

[2] Poyneer, L. A., Dillon, D., Thomas, S., and Macintosh, B. A., "Laboratory demonstration of accurate and efficient nanometer-level wavefront control for extreme adaptive optics," *Applied Optics* **47**, 1317–1326 (Mar. 2008).

[3] Rouan, D., Riaud, P., Boccaletti, A., Clénet, Y., and Labeyrie, A., "The Four-Quadrant Phase-Mask Coronagraph. I. Principle," *PASP* **112**, 1479–1486 (Nov. 2000).

[4] Soummer, R., "Apodized Pupil Lyot Coronagraphs for Arbitrary Telescope Apertures," *ApJ Letter* **618**, L161–L164 (Jan. 2005).

[5] Antichi, J., Dohlen, K., Gratton, R. G., Mesa, D., Claudi, R. U., Giro, E., Boccaletti, A., Mouillet, D., Puget, P., and Beuzit, J.-L., "BIGRE: A Low Cross-Talk Integral Field Unit Tailored for Extrasolar Planets Imaging Spectroscopy," *ApJ* **695**, 1042–1057 (Apr. 2009).

[6] Racine, R., Walker, G. A. H., Nadeau, D., Doyon, R., and Marois, C., "Speckle Noise and the Detection of Faint Companions," *PASP* **111**, 587–594 (May 1999).

[7] Marois, C., Lafrenière, D., Doyon, R., Macintosh, B., and Nadeau, D., "Angular Differential Imaging: A Powerful High-Contrast Imaging Technique," *ApJ* **641**, 556–564 (Apr. 2006).

[8] Vigan, A., Gry, C., Salter, G., Mesa, D., Homeier, D., Moutou, C., and Allard, F., "High-contrast imaging of Sirius A with VLT/SPHERE: looking for giant planets down to one astronomical unit," *MNRAS* **454**, 129–143 (Nov. 2015).

[9] Beuzit, J.-L., Feldt, M., Dohlen, K., Mouillet, D., Puget, P., Wildi, F., Abe, L., Antichi, J., Baruffolo, A., Baudoz, P., Boccaletti, A., Carbillet, M., Charton, J., Claudi, R., Downing, M., Fabron, C., Feautrier, P., Fedrigo, E., Fusco, T., Gach, J.-L., Gratton, R., Henning, T., Hubin, N., Joos, F., Kasper, M., Langlois, M., Lenzen, R., Moutou, C., Pavlov, A., Petit, C., Pragt, J., Rabou, P., Rigal, F., Roelfsema, R., Rousset, G., Saisse, M., Schmid, H.-M., Stadler, E., Thalmann, C., Turatto, M., Udry, S., Vakili, F., and Waters, R., "SPHERE: a 'Planet Finder' instrument for the VLT," in [*SPIE Conference Series*], **7014**, 18 (July 2008).

[10] Petit, C., Sauvage, J.-F., Fusco, T., Sevin, A., Suarez, M., Costille, A., Vigan, A., Soenke, C., Perret, D., Rochat, S., Barrufolo, A., Salasnich, B., Beuzit, J.-L., Dohlen, K., Mouillet, D., Puget, P., Wildi, F., Kasper, M., Conan, J.-M., Kulcsár, C., and Raynaud, H.-F., "SPHERE eXtreme AO control scheme: final performance assessment and on sky validation of the first auto-tuned LQG based operational system," in [*SPIE Conference Series*], **9148**, 0 (Aug. 2014).

[11] Sauvage, J.-F., Fusco, T., Petit, C., Mouillet, D., Dohlen, K., Costille, A., Beuzit, J.-L., Baruffolo, A., Kasper, M., Suarez Valles, M., Downing, M., Feautrier, P., Mugnier, L., and Baudoz, P., "Wave-front sensor strategies for SPHERE: first on-sky results and future improvements," in [*SPIE Conference Series*], **9148** (Aug. 2014).

[12] Hugot, E., Ferrari, M., El Hadi, K., Costille, A., Dohlen, K., Rabou, P., Puget, P., and Beuzit, J. L., "Active optics methods for exoplanet direct imaging. Stress polishing of supersmooth aspherics for VLT-SPHERE planet finder," *A&A* **538**, A139 (Feb. 2012).

[13] Boccaletti, A., Carbillet, M., Fusco, T., Mouillet, D., Langlois, M., Moutou, C., and Dohlen, K., "End-to-end simulation of AO-assisted coronagraphic differential imaging: estimation of performance for SPHERE," in [*SPIE Conference Series*], **7015**, 6 (July 2008).

[14] Claudi, R. U., Turatto, M., Gratton, R. G., Antichi, J., Bonavita, M., Bruno, P., Cascone, E., De Caprio, V., Desidera, S., Giro, E., Mesa, D., Scuderi, S., Dohlen, K., Beuzit, J. L., and Puget, P., "SPHERE IFS: the spectro differential imager of the VLT for exoplanets search," in [*SPIE Conference Series*], **7014**, 3 (July 2008).

[15] Dohlen, K., Langlois, M., Saisse, M., Hill, L., Origne, A., Jacquet, M., Fabron, C., Blanc, J.-C., Llored, M., Carle, M., Moutou, C., Vigan, A., Boccaletti, A., Carbillet, M., Mouillet, D., and Beuzit, J.-L., "The infrared dual imaging and spectrograph for SPHERE: design and performance," in [*SPIE Conference Series*], **7014**, 3 (July 2008).

[16] Vigan, A., Moutou, C., Langlois, M., Allard, F., Boccaletti, A., Carbillet, M., Mouillet, D., and Smith, I., "Photometric characterization of exoplanets using angular and spectral differential imaging," *MNRAS* **407**, 71–82 (Sept. 2010).

[17] Vigan, A., Langlois, M., Moutou, C., and Dohlen, K., "Exoplanet characterization with long slit spectroscopy," *A&A* **489**, 1345–1354 (Oct. 2008).

[18] Vigan, A., N'Diaye, M., and Dohlen, K., "Apodization in high-contrast long-slit spectroscopy. Closer, deeper, fainter, cooler," *A&A* **555**, A49 (July 2013).

[19] N'Diaye, M., Dohlen, K., and Cuevas, S., "Apodized Pupil Lyot Coronagraph, Working without Lyot Stop," in [*Proceedings of the conference In the Spirit of Bernard Lyot: The Direct Detection of Planets and Circumstellar Disks in the 21st Century. June 04 - 08, 2007. University of California, Berkeley, CA, USA. Edited by Paul Kalas.*], Kalas, P., ed. (June 2007).

[20] N'Diaye, M., Cuevas, S., and Dohlen, K., "High contrast imaging feasibility study for FRIDA," in [*SPIE Conference Series*], **7014** (Aug. 2008).

[21] Martinez, P., Dorrer, C., Aller Carpentier, E., Kasper, M., Boccaletti, A., Dohlen, K., and Yaitskova, N., "Design, analysis, and testing of a microdot apodizer for the Apodized Pupil Lyot Coronagraph," *A&A* **495**, 363–370 (Feb. 2009).

[22] Martinez, P., Dorrer, C., Kasper, M., Boccaletti, A., and Dohlen, K., "Design, analysis, and testing of a microdot apodizer for the apodized pupil Lyot coronagraph. II. Impact of the dot size," *A&A* **500**, 1281–1285 (June 2009).

[23] Dorrer, C. and Zuegel, J. D., "Design and analysis of binary beam shapers using error diffusion," *Journal of the Optical Society of America B Optical Physics* **24**, 1268–1275 (June 2007).

[24] Carbillet, M., Bendjoya, P., Abe, L., Guerri, G., Boccaletti, A., Daban, J.-B., Dohlen, K., Ferrari, A., Robbe-Dubois, S., Douet, R., and Vakili, F., "Apodized Lyot coronagraph for SPHERE/VLT. I. Detailed numerical study," *Experimental Astronomy* **30**, 39–58 (May 2011).

[25] Guerri, G., Daban, J.-B., Robbe-Dubois, S., Douet, R., Abe, L., Baudrand, J., Carbillet, M., Boccaletti, A., Bendjoya, P., Gouvret, C., and Vakili, F., "Apodized Lyot coronagraph for SPHERE/VLT: II. Laboratory tests and performance," *Experimental Astronomy* **30**, 59–81 (May 2011).

[26] Hinkley, S., Oppenheimer, B. R., Zimmerman, N., Brenner, D., Parry, I. R., Crepp, J. R., Vasisht, G., Ligon, E., King, D., Soummer, R., Sivaramakrishnan, A., Beichman, C., Shao, M., Roberts, L. C., Bouchez, A., Dekany, R., Pueyo, L., Roberts, J. E., Lockhart, T., Zhai, C., Shelton, C., and Burruss, R., "A New High Contrast Imaging Program at Palomar Observatory," *PASP* **123**, 74–86 (Jan. 2011).

[27] Macintosh, B., Graham, J. R., Ingraham, P., Konopacky, Q., Marois, C., Perrin, M., Poyneer, L., Bauman, B., Barman, T., Burrows, A. S., Cardwell, A., Chilcote, J., De Rosa, R. J., Dillon, D., Doyon, R., Dunn, J., Erikson, D., Fitzgerald, M. P., Gavel, D., Goodsell, S., Hartung, M., Hibon, P., Kalas, P., Larkin, J., Maire, J., Marchis, F., Marley, M. S., McBride, J., Millar-Blanchaer, M., Morzinski, K., Norton, A., Oppenheimer, B. R., Palmer, D., Patience, J., Pueyo, L., Rantakyro, F., Sadakuni, N., Saddlemyer, L., Savransky, D., Serio, A., Soummer, R., Sivaramakrishnan, A., Song, I., Thomas, S., Wallace, J. K., Wiktorowicz, S., and Wolff, S., "First light of the Gemini Planet Imager," *Proceedings of the National Academy of Science* **111**, 12661–12666 (Sept. 2014).

[28] Vigan, A., N'Diaye, M., and Dohlen, K., "Stop-less Lyot coronagraph for exoplanet characterization: design, manufacturing, and tests of the apodizer," in [*SPIE Conference Series*], **9151**, 1 (July 2014).

[29] Sivaramakrishnan, A., Soummer, R., Carr, G. L., Dorrer, C., Bolognesi, A., Zimmerman, N., Oppenheimer, B. R., Roberts, R., and Greenbaum, A., "Calibrating IR optical densities for the Gemini Planet Imager extreme adaptive optics coronagraph apodizers," in [*SPIE Conference Series*], **7440**, 1 (Aug. 2009).

[30] Wildi, F., Mouillet, D., Beuzit, J.-L., Feldt, M., Dohlen, K., Fusco, T., Petit, C., Desidera, S., Gratton, R., Schmid, H.-M., Langlois, M., Vigan, A., Charton, J., Claudi, R., Roelfsema, R., Baruffolo, A., and Puget, P., "Calibrating SPHERE, the exo-planet imager for the VLT," in [*SPIE Conference Series*], **7440**, 0 (Aug. 2009).

[31] Pavlov, A., Möller-Nilsson, O., Feldt, M., Henning, T., Beuzit, J.-L., and Mouillet, D., "SPHERE data reduction and handling system: overview, project status, and development," in [*SPIE Conference Series*], **7019**, 39 (July 2008).

[32] Vigan, A., N'Diaye, M., Dohlen, K., Beuzit, J.-L., Costille, A., Caillat, A., Baruffolo, A., Blanchard, P., Carle, M., Ferrari, M., Fusco, T., Gluck, L., Hugot, E., Jaquet, M., Langlois, M., Le Mignant, D., Llored, M., Madec, F., Mouillet, D., Origné, A., Puget, P., Salasnich, B., and Sauvage, J.-F., "Apodization in high-contrast long-slit spectroscopy. II. Concept validation and first on-sky results with VLT/SPHERE," *A&A* **586**, A144 (Feb. 2016).

[33] N'Diaye, M., Dohlen, K., Fusco, T., and Paul, B., "Calibration of quasi-static aberrations in exoplanet direct-imaging instruments with a Zernike phase-mask sensor," *A&A* **555**, A94 (July 2013).

[34] N'Diaye, M., Dohlen, K., Caillat, A., Costille, A., Fusco, T., Jolivet, A., Madec, F., Mugnier, L., Paul, B., Sauvage, J.-F., Soummer, R., Vigan, A., and Wallace, J. K., "Design optimization and lab demonstration of ZELDA: a Zernike sensor for near-coronagraph quasi-static measurements," in [*SPIE Conference Series*], **9148**, 5 (Aug. 2014).

[35] Dohlen, K., Wildi, F. P., Puget, P., Mouillet, D., and Beuzit, J.-L., "SPHERE: Confronting in-lab performance with system analysis predictions," in [*Second International Conference on Adaptive Optics for Extremely Large Telescopes. Online at http://ao4elt2.lesia.obspm.fr, id.75*], 75 (Sept. 2011).

[36] Biller, B. A., Close, L. M., Masciadri, E., Nielsen, E., Lenzen, R., Brandner, W., McCarthy, D., Hartung, M., Kellner, S., Mamajek, E., Henning, T., Miller, D., Kenworthy, M., and Kulesa, C., "An Imaging Survey for Extrasolar Planets around 45 Close, Young Stars with the Simultaneous Differential Imager at the Very Large Telescope and MMT," *ApJ* **173**, 143–165 (Nov. 2007).

[37] Soummer, R., Pueyo, L., and Larkin, J., "Detection and Characterization of Exoplanets and Disks Using Projections on Karhunen-Loève Eigenimages," *ApJ Letter* **755**, L28 (Aug. 2012).